Energy Advances

ROYAL SOCIETY OF CHEMISTRY

PAPER

View Article Online
View Journal | View Issue

Cite this: *Energy Adv.*, 2022, 1, 697

A metal-free reduced graphene oxide coupled covalent imine network as an anode material for lithium-ion batteries†

Sujan Mondal, ‡[a] Santu Ruidas,‡[a] Kruti K. Halankar,[b] Balaji P Mandal,[b] Sasanka Dalapati[c] and Asim Bhaumik *[a]

Received 17th June 2022,
Accepted 29th August 2022

DOI: 10.1039/d2ya00148a

rsc.li/energy-advances

Organic electrodes for batteries have been receiving tremendous impetus in the recent past for sustainable development. A metal-free crystalline and porous covalent imine network (Tp-THzT-CIN) has been synthesized *via* solvothermal Schiff-base condensation between a trialdehyde (Tp) and a triamine (THzT). This network is laden with lithium ion exchange sites, accessible open pores, high specific surface area and the presence of heteroatoms that enable lithium ions to intercalate into the pores. When explored as an anode material for lithium ion batteries it exhibits a specific capacity of 82 mA h g^{-1} at a current density of 50 mA g^{-1}. Interestingly, when this CIN material is coupled with reduced graphene oxide (rGO), its efficiency has been enhanced many fold and it exhibits a specific capacity of 123 mA h g^{-1} at a current density of 50 mA g^{-1}.

Introduction

Environmental pollution is becoming inevitable since we repeatedly consume non-renewable energy resources for our daily needs. Moreover, the exhaustion of fossil fuels imparts a serious threat to future generations in terms of a sustainable energy resource. Thus, to mitigate these issues and to make an environmentally sustainable energy resource, we must shift our dependency from fossil fuels by adopting renewable energy sources, which has great potential to meet our future energy needs. Renewable energy sources produce electricity intermittently, so it is imperative to develop efficient electrochemical energy storage systems (EESs). Among such systems, rechargeable batteries have emerged as a better storage technique of electricity in the form of chemical energy and applied as the major power supplies in portable devices and electric vehicles. Rechargeable lithium-ion batteries (LIBs)[1–4] have proved themselves a promising candidate of such sustainable energy storage systems and revolutionized electronic devices as the dominating power supplier owing to their underlying merits of high-energy, high-power density, long cycle life and low rate of self-discharge. However, substantial improvements in the electrochemical performance of LIBs are still needed to meet practical demands of high energy and power. There are a number of inorganic anode materials known so far due to their good electrochemical performance. But high cost, toxicity and non-renewability are some shortcomings that limit their usage to some extent.[5–12]

Therefore, researchers are endeavoring to make a more updated version of LIBs by introducing alternate and metal-free electrode materials for the next generation of "green battery". Nowadays, organic materials[13–17] have been extensively explored as electrode materials due to their flexibility in design and synthesis, structural diversity, and resource renewability. Again, their uses are limited by dissolution problems and side reactions. Insoluble organic polymers as electrode materials have resolved this dissolution problem to some extent. In the meantime, symbiosis of porous organic polymers with carbon-based materials such as rGO[18,19] is an effective strategy to get novel anode materials for good electrochemical performance, since they have excellent electronic conductivity, and high storage capacity as the lithium ions can accommodate on both sides of the sheet[20] and also can bind to defect sites[21] of rGO.

In the field of nanoscience, nanomaterials with different particle dimensions have received considerable interest for widespread applications[22–29] due to their structural characteristics, such as enormous surface area, outstanding stabilities and customized features. In particular, imine-based porous

[a] *School of Materials Sciences, Indian Association for the Cultivation of Science, Jadavpur, Kolkata 700032, India. E-mail: msab@iacs.res.in*
[b] *Chemistry Division, Bhabha Atomic Research Centre, Mumbai - 400085, India*
[c] *Department of Materials Science, School of Technology, Central University of Tamil Nadu (CUTN), Thiruvarur-610005, Tamil Nadu, India*

† Electronic supplementary information (ESI) available: Materials, methods and characterization tools, ^{1}H and ^{13}C NMR of the monomers, Pawley refined powder X-ray profile with other related data, FTIR spectra, TGA profile of Tp-THzT-CIN, energy dispersive X-ray (EDX) spectroscopy, Raman spectra. See DOI: https://doi.org/10.1039/d2ya00148a

‡ SM and SR contributed equally to this paper.

materials[25–28] have gained significant attention and emerged as one of the most often used polymeric backbones in this area. There is a legitimate reason for this interest: imine condensations are straightforward, linked by strong covalent bonds, and can occur under mild conditions that enable the easy production of functionalized materials. A number of imine-linked porous networks have been reported for energy applications, such as super capacitors,[24] metal ion batteries,[24–27] water splitting[28] and so on. However, porous π-conjugated polymers bearing cation exchangeable sites are highly suitable for Li^+ exchange and void spaces present in those frameworks facilitate storage for the lithium ions.[25–27,30–32] In that endeavor, to design novel porous organic materials, we aim to introduce a crystalline covalent imine network (Tp-THzT-CIN)[28,33,34] through the execution of the Schiff-base condensation reaction between 1,3,5-triformylphloroglucinol and 2,4,6-trihydrazinyl-1,3,5-triazine (THzT) as an anode material. Owing to their porous nature, crystallinity, extended conjugation throughout the framework and most importantly being enriched with lithium-ion exchangeable sites that accelerate the intercalation of lithium ions in the pores of the material, they can offer huge opportunities in LIBs. This CIN electrode shows a noticeable specific capacity of 82 mA h g^{-1} at a current density of 50 mA g^{-1}. Interestingly, an enhancement in specific capacity of 123 mA h g^{-1} was observed when CIN is coupled with reduced graphene oxide (rGO).

Experimental procedure

1,3,5-Triformylphloroglucinol (Tp)

1,3,5-Triformylphloroglucinol was prepared following the previously reported procedure.[35] In short, 80 mL of trifluoroacetic acid was added to a mixture of phloroglucinol (6 g) and hexamethylenetetramine (15 g) under ice-cold conditions. Then the system was allowed to reach room temperature and the temperature was raised to 100 °C for 3 h. After cooling to room temperature, 300 mL 3 M HCl was added and stirring was continued overnight. Finally, the mixture was filtered through a Celite bed and the filtrate was extracted with dichloromethane 3 times. After evaporation, the salmon-coloured solid was purified with ethanol. Yield: 19%. ^{1}H NMR (400 MHz, $CDCl_3$) δ 14.12 (s, 3H); 10.15 (s, 3H), Fig. S1, ESI.† ^{13}C NMR ($CDCl_3$, 100 MHz): 192.4, 173.9, 103.1 ppm (Fig. S2, ESI†).

2,4,6-Trihydrazinyl-1,3,5-triazine (THzT)

The THzT amine was synthesized by the following literature method.[36] To a stirred solution of hydrazine hydrate (5 mL) in acetonitrile, suspended cyanuric chloride (369 mg, 2 mmol) in 200 mL acetonitrile was added over 45 min at room temperature. The addition of cyanuric chloride caused an immediate formation of precipitate. The reaction mixture was then boiled under reflux conditions for 5 h. The resulting mixture was filtered and thoroughly washed with excess acetonitrile. Yield: 83%. ^{13}C NMR ($CDCl_3$, 100 MHz): 151.1 ppm (Fig. S3, ESI†). Selected FTIR peaks (KBr cm^{-1}): 3299, 1587, 1556, 1487.

Tp-THzT-CIN

The synthetic procedure was executed through the Schiff-base condensation of 1,3,5-triformylphloroglucinol (210 mg, 1 mmol) and 2,4,6-trihydrazinyl-1,3,5-triazine (220 mg, 1 mmol) in 5 mL of 1 : 1 mesitylene:dioxane in the presence of 6 M acetic acid in a pyrex tube. At first, the reaction mixture was loaded into a pyrex tube and sonicated for 20 min. After that, the reaction system was degassed through freeze–pump–thaw cycles three times and then the tube was vacuum flame sealed. Next, the tube containing the reaction mixture was kept in an oven at 120 °C for 3 days. The resulting red-coloured material was collected through filtration and successively washed with methanol, acetone, dichloromethane and tetrahydrofuran, respectively. The final material was dried under vacuum at 100 °C overnight.

Synthesis of CIN–rGO

The as-prepared Tp-THzT-CIN was ground thoroughly with 5% of reduced graphene oxide sheets and then heated in a vacuum oven for 8 h at 90 °C. This sample is the covalent-imine network anchored on reduced graphene oxide sheets, which is named as CIN–rGO henceforth.

Electrochemical measurements

The electrochemical studies of the as-synthesised Tp-THzT-CIN and CIN–rGO samples were performed by using a CR2032 type coin cell with lithium metal foil as both the reference and counter electrode. The working electrode was prepared using active material (Tp-THzT-CIN and CIN–rGO), carbon black (CB) and polyvinylidene fluoride (PVDF) in the ratio 6 : 3 : 1, respectively. This mixture was ground thoroughly in the presence of NMP for 30 min to obtain a uniform slurry. This slurry was coated on clean copper foil (current collector) and was further dried in a vacuum oven at 90 °C for about 12 h. These electrodes were used for assembling the cell in an argon filled glove box (Mbraun). The mass loading of active material in the electrode was ~2 mg. The non-aqueous electrolyte used was 1 M LiPF6 dissolved in an ethylene carbonate (EC) and dimethyl carbonate (DMC) mixture (1 : 1, in wt%). The prepared electrode was cycled against lithium metal as a counter electrode. Cyclic voltammetry (CV) was performed using an electrochemical workstation (Origalys, France) at different scan rates at room temperature. The galvanostatic charge–discharge tests were recorded using a multi-channel battery testing system (NEWARE) with a cut off voltage of 0.01–3.00 V *versus* Li/Li^+. The electrochemical impedance of the coin cells was measured using Novocontrol's Alpha A high frequency analyser. Impedance was measured with ac voltage 70 mV in the frequency range 1 Hz to 1 MHz at room temperature. The specific capacity is calculated based on the total weight of the active material.

Results and discussion

The covalent imine network material Tp-THzT-CIN was prepared by the extended condensation reaction of 1,3,5-triformylphloroglucinol (Tp) and 2,4,6-trihydrazinyl-1,3,5-triazine (THzT)

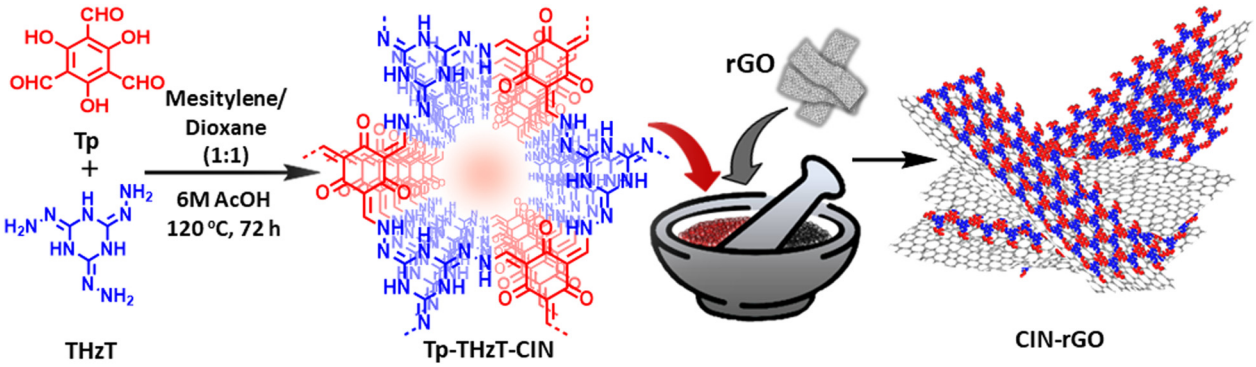

Scheme 1 Schematic illustration of the synthesis of Tp-THzT-CIN and the CIN–rGO composite material.

(Scheme 1) under solvothermal conditions. To accelerate the polymerization process, 6 M acetic acid was used as an acid catalyst. The resultant burgundy red solid of CIN (Yield: 79%) was found to be insoluble in most of the common organic solvents and it was thermally stable up to ~200 °C as revealed by thermogravimetric analysis (Fig. S4, ESI†). Elemental analysis of this CIN confirms the adequacy of nitrogen (33.83%) in support for good matching of the experimental C, H and N values with the theoretical ones. The π-conjugated 2D CIN material was further mixed with 5% of reduced GO to form a CIN–rGO composite prior to use as an electrode material in lithium-ion battery applications.

The crystallinity as well as phase purity of Tp-THzT-CIN have been validated by powder X-ray diffraction (PXRD) analysis. As shown in Fig. 1a, an intense peak appeared at a 2θ of 7.98° corresponding to its (100) plane and another set of diffraction peaks at 11.81 and 27.02°, respectively are attributed to the reflection from the 110 and 220 planes. Considering the connecting pattern of monomers, a feasible 2D model structure was generated using Accelrys BIOVIA material studio software. The simulated PXRD pattern of the geometrically optimized AA stacking model was found to be congruent with the experimental PXRD pattern of Tp-THzT-CIN. The Pawley refinement was further accomplished in favour of supportive crystallographic profile pattern analysis from the experimental X-ray pattern. After refining the structure, the trigonal space group $P\bar{6}$ was determined with unit cell parameters and good agreement factors ($a = b = 12.73$ Å, $c = 3.33$ Å, $\alpha = \beta = 90°$, $\gamma = 120°$, $R_{wp} = 5.86\%$ and $R_p = 4.61\%$). The details of the refinement results have been given in Fig. S5, S6 and Table S1, ESI.† All the diffraction patterns of CIN–rGO composite are resembling Tp-THzT-CIN, which demonstrates that the CIN based target material was properly synthesized. However, the presence of graphene in the CIN–rGO composites weakens the peak intensity somewhat. Furthermore, the broad peak at 24.9° (2θ) of rGO slightly shifted to higher 2θ value (25.6°) for the rGO–CIN composite, suggesting that individual rGO layers are clothed with CIN, which reduced the interplanar spacing of the rGO layers.[37]

The FTIR spectra for all the samples were collected and presented in Fig. S7, ESI.† The FTIR spectrum of Tp-THzT-CIN does not contain any aldehydic and primary amine stretching frequencies, which indicates that complete consumption of the monomers took place. The FTIR spectra for CIN and the CIN–rGO composite showed similar absorption stretching bands. The characteristic stretching bands at 1616 (C═O), 1590 (C═C) and 1280 (C–N) cm^{-1} could be attributed to successful formation of β-ketoenamine-linked CIN networks.[38,39] The characteristic D and G band of reduced graphene oxide was observed at 1353 and 1580 cm^{-1} in the Raman spectrum of the CIN–rGO composite (Fig. S8, ESI†), which suggests the presence

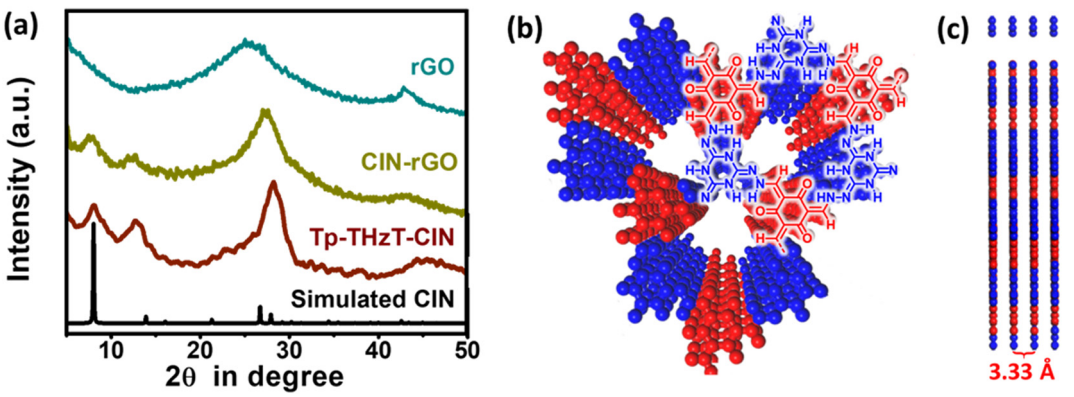

Fig. 1 (a) PXRD patterns of rGO, Tp-THzT-CIN and the CIN–rGO composite compared with a theoretical XRD pattern from a geometrically optimized AA stacked model structure. Top (b) and side view (c) of the space-filled model with ideal eclipsed (AA) packing.

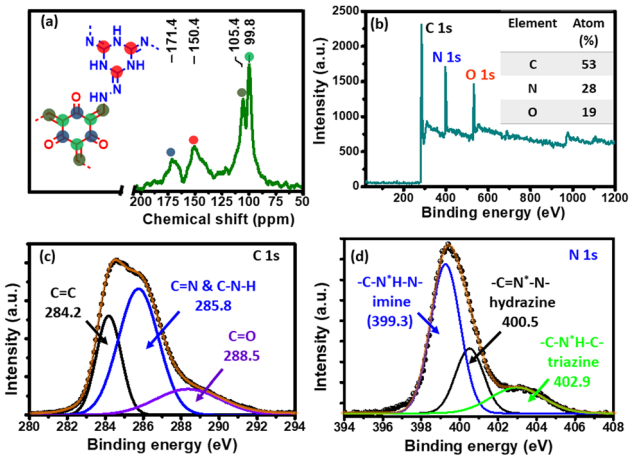

Fig. 2 (a) Solid-state ^{13}C MAS NMR spectrum of the Tp-THzT-CIN material (different carbon nuclei are marked by different coloured dots). (b) XPS survey spectrum of Tp-THzT-CIN. Deconvoluted high resolution XPS spectra of C 1s (c) and N 1s (d) of the pristine CIN material.

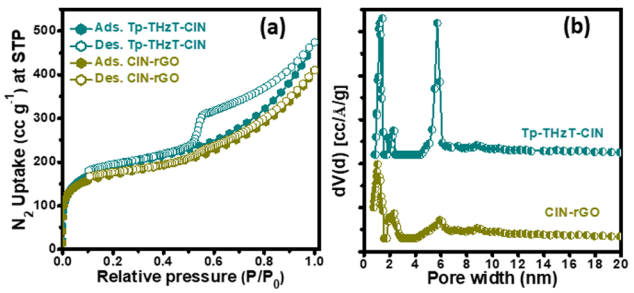

Fig. 3 (a) Nitrogen adsorption and desorption isotherms of the Tp-THzT-CIN and CIN–rGO composite with their corresponding pore size distribution (PSD) plots (b).

of rGO in the composite material. To understand the structural growth and chemical environment of different carbon nuclei of the CIN, a ^{13}C solid NMR study was carried out. The resonance peaks at 150.45 and 171.38 ppm in Fig. 2a are assigned to enamine (C═N) and carbonyl (C═O) carbon, respectively, which signifies that the CIN framework is formed by thermodynamically favourable β-ketoenamine linkage.[40,41] On the other hand, signals at 105.38 and 99.75 ppm are due to the aromatic carbon of a tri-aldehyde ring and triazine ring carbon, respectively.

X-Ray photoelectron spectroscopy (XPS) was further used to investigate the chemical state of the elements and their composition in the CIN skeleton. As seen from Fig. 2b, three clear distinct peaks of C 1s, N 1s and O 1s are visible. The deconvoluted high resolution C 1s XPS spectrum (Fig. 2c) displayed mainly four components at 284.2 eV (C═C), 285.8 eV (triazine and imine carbon) and 288.5 eV (C═O), respectively. The high-resolution N 1s core level spectrum (Fig. 2d) can be divided into three well resolved peaks, *i.e.*, imine nitrogen (C–N*H–N, 399.3 eV), hydrazine nitrogen (C═N*–N, 400.5 eV), and triazine nitrogen (C–N*H–C, 402.9 eV).

The specific surface area and porosity of the Tp-THzT-CIN and CIN–rGO composites were assessed by N_2 adsorption–desorption measurement at 77 K on the activated sample. As shown in Fig. 3a, the adsorption isotherm contains a combination type I and type IV isotherms, which unambiguously indicates hierarchical porosity with both micropores and mesopores in the material.[42,43] The Brunauer–Emmett–Teller indicates that Tp-THzT-CIN has a surface area of 697 $m^2\ g^{-1}$. The coexistence of micropores and mesopores in the CIN network was further confirmed from the bimodal pore size distribution (PSD) plot, as shown in Fig. 3b. This PSD was measured on the basis of non-local density functional theory

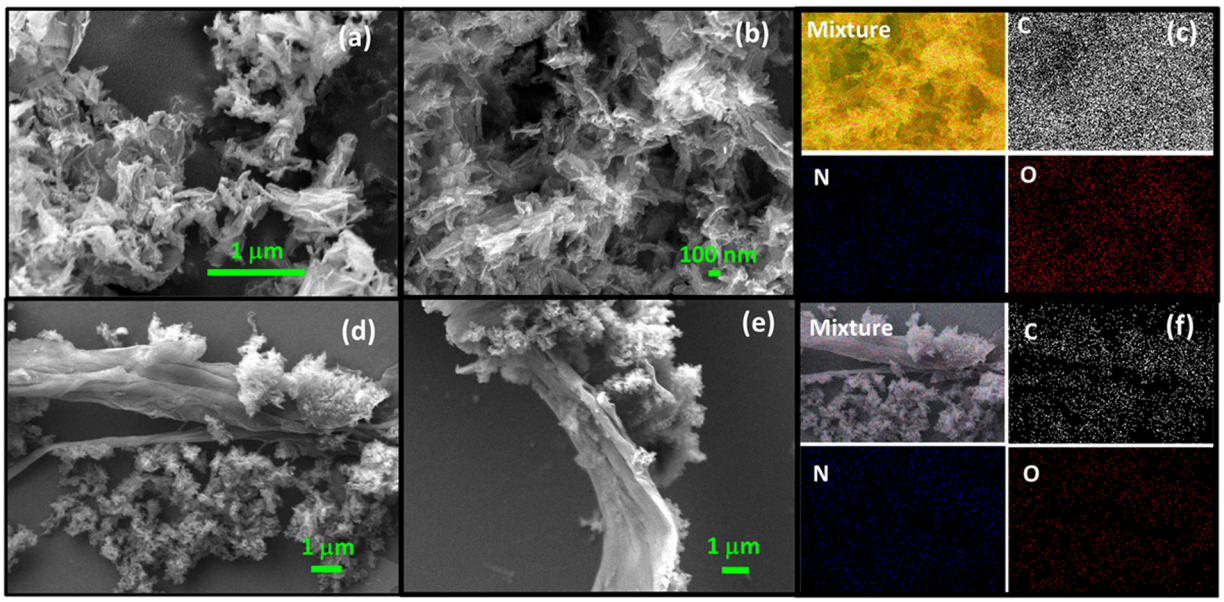

Fig. 4 SEM images of Tp-THzT-CIN (a and b) and the composite material (d and e). The distribution of C, N and O elements is shown in the respective elemental mapping images for the Tp-THzT-CIN (c) and CIN–rGO (f) composite materials.

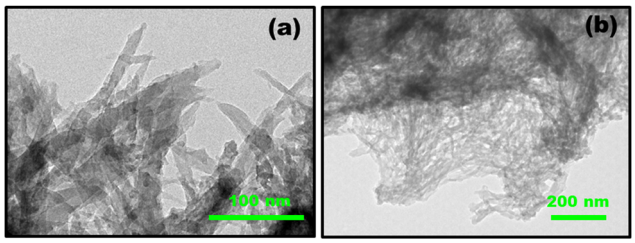

Fig. 5 HRTEM images of the Tp-THzT-CIN material (a and b) at different magnifications.

(NLDFT) and it signifies the presence of pores of sizes 1.4 and 5.7 nm with a total pore volume of 0.698 g cm^{-3}. From the simulated AA stacked model of Tp-THzT-CIN, the measured pore diameter is 1.3 nm, which is close to the experimental pore diameter obtained from N_2-sorption analysis (1.4 nm). The observed mesoporosity in the pristine CIN material could be attributed to the interparticle voids that are generated during the agglomeration of the flake-like clusters (Fig. 4a, b and 5a, b) of CIN. On the contrary, the CIN–rGO composite has to some extent less specific surface area (644 m^2 g^{-1}) with a typical type I isotherm. In the CIN–rGO composite material, rGO is stacked in between the CIN particles, which may contribute to the reduction of the surface area and pore size.

Scanning (Fig. 4a and b) and transmission electron microscopy images (Fig. 5) established that Tp-THzT-CIN has the morphology of flake-like clusters, made up of nanorods with serious agglomeration. Noticeably, in the composite material, the coexistence of sheet and flake-like morphologies of both rGO and the CIN material are observed (Fig. 4d and e). The elemental distributions in both the pristine CIN and CIN–rGO composite samples were examined for further clarification, and a homogenous

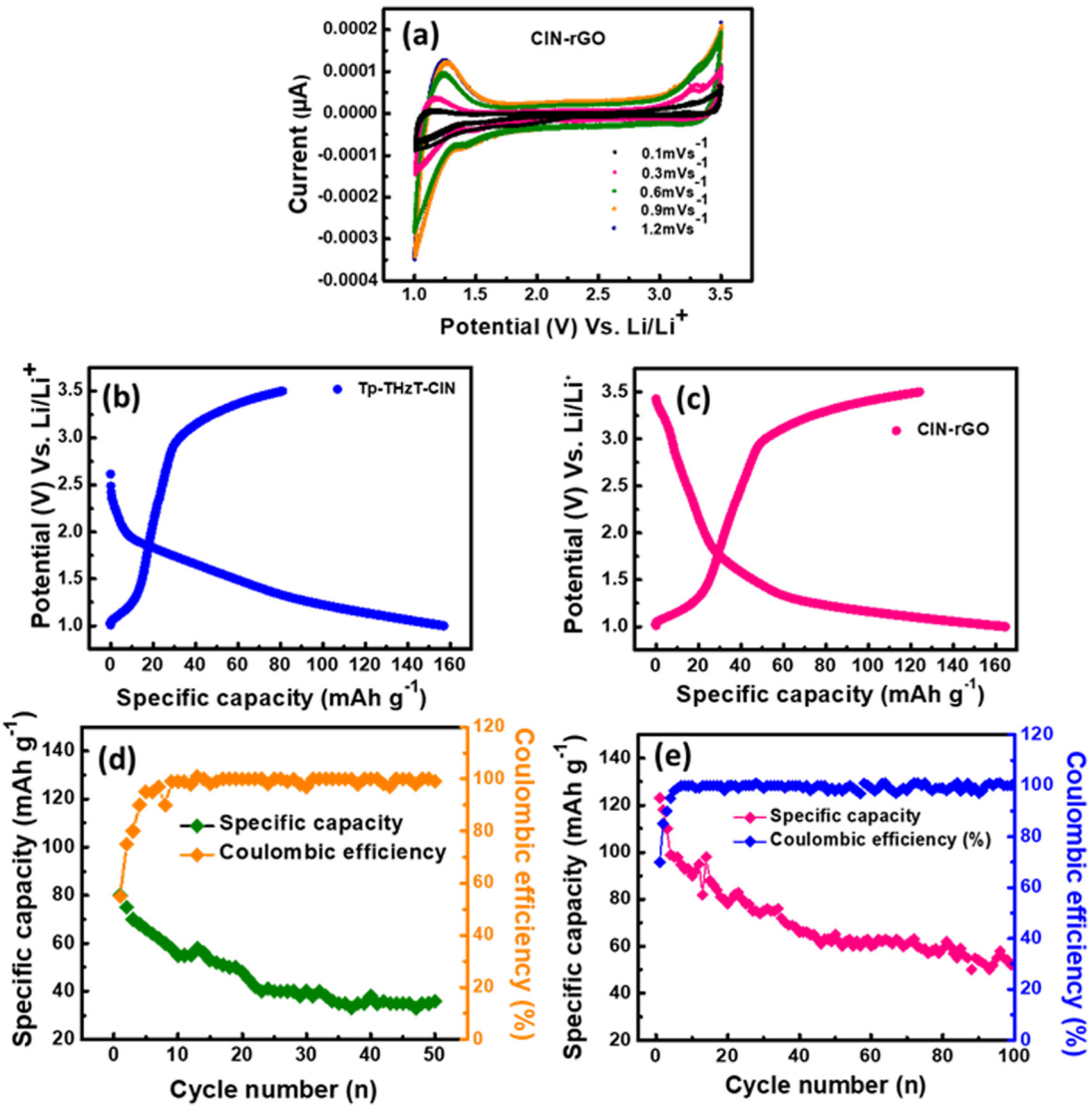

Fig. 6 (a) Cyclic voltammograms of CIN–rGO cycled at different scan rates of 0.1, 0.3, 0.6, 0.9 and 1.2 mV s^{-1} between 1–3.5 V. Initial charge discharge curves at 50 mA g^{-1} current density of Tp-THzT-CIN (b) and CIN–rGO (c). Cycling performance test at 50 mA g^{-1} current density of Tp-THzT-CIN (d) and CIN–rGO (e).

distribution of C, N, and O atoms is exhibited throughout the materials (Fig. 4c, f and Fig. S9, ESI†). The thermal analysis of the preheated material was conducted in air (Fig. S4, ESI†) and reveals that no significant weight loss was observed with the increase in temperature up to 200 °C, which indicates that the porous framework is stable up to this temperature and beyond this temperature considerable weight loss occurred that could be attributed to the decomposition of the organic moieties in the framework.

Cyclic voltammetr

To understand the physical/chemical behaviour of the electrode samples during charge–discharge cycling, cyclic voltammetry (CV) measurements were performed.[44] Cyclic voltammograms were recorded for Tp-THzT-CIN and CIN–rGO electrodes at different scan rates of 0.1, 0.3, 0.6, 0.9 and 1.2 mV s^{-1} in the potential range of 1.0–3.5 V (Fig. 6a). A redox couple could be observed at 1.42/3.27 V. The cyclic voltammetry studies suggest that the electrode material undergoes a reversible Li-ion intercalation/deintercalation process.

Electrochemical studies

The covalent imine network (Tp-THzT-CIN) structure has lots of lithium-ion exchangeable sites. Therefore, it is expected to be an electrode material for futuristic lithium-ion batteries. The electrochemical performance with regard to the Li insertion/extraction process has been thoroughly investigated.[45] Fig. 6b and c show the initial discharge and charge profiles of the Tp-THzT-CIN and CIN–rGO electrodes at a current density of 50 mA g^{-1} in the potential range of 3.0–0.01 V *vs.* Li/Li^+. The CIN–rGO electrode delivers an initial specific capacity of 123 mA h g^{-1} at 50 mA g^{-1} with a coulombic efficiency of ~87%, whereas the Tp-THzT-CIN electrode shows 82 mA h g^{-1} at a current density of 50 mA g^{-1} with coulombic efficiency ~79% (Fig. 6b and c). The coulombic efficiency improved to ~100% after the first 5 cycles in both the samples. A cycling test was performed for both the electrodes Tp-THzT-CIN and CIN–rGO for 50 cycles and 100 cycles at 50 mA g^{-1}, as shown in Fig. 6d and e. The electrochemical performance of Tp-THzT-CIN improves upon addition of rGO due to the higher electrical conductivity of rGO.[46]

Another important aspect of any electrode material is its performance under different current densities. CIN–rGO showed superior performance with a capacity of 123, 84 and 45 mA h g^{-1} at 50 mA g^{-1}, 75 mA g^{-1} and 100 mA g^{-1} current density, respectively. On the other hand, the performance of pristine CIN at different current densities has been investigated. The specific capacity of pristine CIN is found to be inferior in comparison with the CIN–rGO composite (Fig. S10, ESI†). Electrochemical impedance spectroscopy (EIS) analysis is a well-known technique used to study the transport kinetics of electrodes in lithium-ion batteries. In the present case, EIS has also been performed for both the samples in the discharged state after two charge–discharge cycles. The Nyquist plots of the Tp-THzT-CIN and CIN–rGO samples have been presented in Fig. 7. Both the samples show two depressed semicircles at the high frequency and mid frequency region. A sloping line

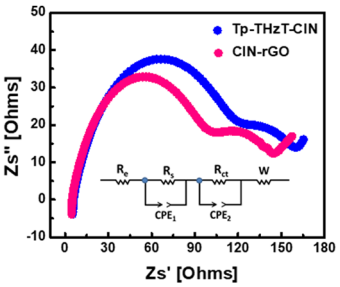

Samples	R_e	R_s	R_{ct}
Tp-THzT-CIN	6.2	132.5	189.3
CIN-rGO	4.3	115.2	172.1

Fig. 7 Impedance plots of the samples Tp-THzT-CIN and CIN–rGO. The model used to fit the impedance is shown in the plot. In the model, R_e corresponds to electrolyte resistance, R_s corresponds to SEI film resistance, CPE1 is the constant phase element of the SEI film, R_{ct} is charge transfer resistance and CPE2 is the constant phase element for charge transfer.

corresponding to Warburg resistance could also be observed in the low frequency region. This depressed curve is attributed to a charge transfer process and Warburg resistance is related to the mass transfer of lithium ions. The plot clearly shows that the diameter of the semicircle for the CIN–rGO electrode in the high frequency region is smaller than that of the Tp-THzT-CIN electrode, which indicates that the CIN–rGO electrode possesses lower contact and charge-transfer impedances. Here, the CIN–rGO electrode acts as an efficient charge carrier and facilitates the charge transfer process at the interface resulting in higher specific capacity.

Conclusions

We report a crystalline covalent imine network material Tp-THzT-CIN through the Schiff base condensation of 1,3,5-triformylphloroglucinol and 2,4,6-trihydrazinyl-1,3,5-triazine. Tp-THzT-CIN is found to be crystalline in nature with good thermal stability and high specific surface area making it suitable as an electrode material for lithium-ion batteries. It has several lithium-ion exchangeable sites (–OH and –NH), which is a pre-requisite for electrode materials for Li-ion batteries. The CIN–rGO composite shows superior electrochemical performance as rGO enhances the electronic conductivity. The excellent specific capacity and its retention over several cycles in the CIN–rGO 2D/2D nanocomposite material suggested its huge potential to be explored as an energy storage material in the future.

Conflicts of interest

There are no conflicts to declare.

Acknowledgements

SM and SR acknowledge CSIR, New Delhi, India. AB would like to thank DST, New Delhi for funding through Indo-Russian project (DST/INT/RUS/P-25). Assistance from CSS, IACS Kolkata is acknowledged.

Notes and references

1 M. Armand and J. M. Tarascon, *Nature*, 2008, **451**, 652–657.
2 Y. Liang, Z. Tao and J. Chen, *Adv. Energy Mater.*, 2012, **2**, 742–769.
3 A. Masias, J. Marcicki and W. A. Paxton, *ACS Energy Lett.*, 2021, **6**, 621–630.
4 L. Li, D. Zhang, J. Deng, Y. Gou, J. Fang, H. Cui, Y. Zhao and M. Cao, *Carbon*, 2021, **183**, 721–734.
5 D. H. P. Kang, M. Chen and O. A. Ogunseitan, *Environ. Sci. Technol.*, 2013, **47**, 5495–5503.
6 L. Croguennec and M. R. Palacin, *J. Am. Chem. Soc.*, 2015, **137**, 3140–3156.
7 M. Okubo, E. Hosono, J. Kim, M. Enomoto, N. Kojima, T. Kudo, H. Zhou and I. Honma, *J. Am. Chem. Soc.*, 2007, **129**, 7444–7452.
8 A. Rougier, P. Gravereau and C. Delmas, *J. Electrochem. Soc.*, 2019, **143**, 1168.
9 J. Zhang, F. Cheng, S. Chou, J. Wang, L. Gu, H. Wang, H. Yoshikawa, Y. Lu and J. Chen, *Adv. Mater.*, 2019, **31**, 1901808.
10 M. V. Reddy, T. W. Jie, C. J. Jafta, K. I. Ozoemena, M. K. Mathe, A. S. Nair, S. S. Peng, M. S. Idris, G. Balakrishna, F. I. Ezema and B. V. R. Chowdari, *Electrochim. Acta*, 2014, **128**, 192–197.
11 L. Geng, J. Liu, D. L. Wood, Y. Qin, W. Lu, C. J. Jafta, Y. Bai and I. Belharouak, *ACS Appl. Energy Mater.*, 2020, **3**, 7058–7065.
12 F. P. Nkosi, C. J. Jafta, M. Kebede, M. L. le Roux, M. K. Mathe and K. I. Ozoemena, *RSC Adv.*, 2015, **5**, 32256.
13 S. Zhang, S. Ren, D. Han, M. Xiao, S. Wang, L. Sun and Y. Meng, *ACS Appl. Mater. Interfaces*, 2020, **12**, 36237–36246.
14 H. Lyu, X.-G. Sun and S. Dai, *Adv. Energ. Sustain. Res.*, 2021, **2**, 2000044.
15 J. Ren, X. Wang, H. Liu, Y. Hu, X. Zhang and T. Masuda, *React. Funct. Polym.*, 2020, **146**, 104365.
16 H. Alt, H. Binder, A. Köhling and G. Sandstede, *Electrochim. Acta*, 1972, **17**, 873–887.
17 D. Lin, Y. Liu, Z. Liang, H.-W. Lee, J. Sun, H. Wang, K. Yan, J. Xie and Y. Cui, *Nat. Nanotechnol.*, 2016, **11**, 626–632.
18 S. N. Alam, N. Sharma and L. Kumar, *Graphene*, 2017, **06**, 1–18.
19 D. C. Marcano, D. V. Kosynkin, J. M. Berlin, A. Sinitskii, Z. Sun, A. S. Slesarev, L. B. Alemany, W. Lu and J. M. Tour, *ACS Nano*, 2018, **12**, 2078.
20 N. A. Kaskhedikar and J. Maier, *Adv. Mater.*, 2009, **21**, 2664–2680.
21 D. Pan, S. Wang, B. Zhao, M. Wu, H. Zhang, Y. Wang and Z. Jiao, *Chem. Mater.*, 2009, **21**, 3136–3142.
22 S. Bej, S. Mandal, A. Mondal, T. K. Pal and P. Banerjee, *ACS Appl. Mater. Interfaces*, 2021, **13**, 25153–25163.
23 D. Dey, N. C. Murmu and P. Banerjee, *RSC Adv.*, 2019, **9**, 7469–7478.
24 S. Kandambeth, V. S. Kale, O. Shekhah, H. N. Alshareef and M. Eddaoudi, *Adv. Energy Mater.*, 2022, **12**, 2100177.
25 C. Wei, L. Tan, Y. Zhang, K. Zhang, B. Xi, S. Xiong, J. Feng and Y. Qian, *ACS Nano*, 2021, **15**, 12741–12767.
26 K. Zhang, K. O. Kirlikovali, R. S. Varma, Z. Jin, H. W. Jang, O. K. Farha and M. Shokouhimehr, *ACS Appl. Mater. Interfaces*, 2020, **12**, 27821–27852.
27 L. Fang, X. Cao and Z. Cao, *J. Phys.: Condens. Matter*, 2019, **31**, 205502.
28 S. Mondal, B. Mohanty, M. Nurhuda, S. Dalapati, R. Jana, M. Addicoat, A. Datta, B. K. Jena and A. Bhaumik, *ACS Catal.*, 2020, **10**, 5623–5630.
29 R. Das, R. Pal, S. Bej, M. Mondal, K. Kundu and P. Banerjee, *Mater. Adv.*, 2022, **3**, 4421–4459.
30 W. Zhao, F. Zhang, L. Y. Yang, S. Bi, D. Q. Wu, Y. F. Yao, M. Wagner, R. Graf, M. R. Hansen, X. D. Zhuang and X. L. Feng, *J. Mater. Chem. A*, 2016, **4**, 15162–15168.
31 R. Merkle, P. Gutbrod, P. Reinold, M. Katzmaier, R. Tkachov, J. Maier and S. Ludwigs, *Polymer*, 2017, **132**, 216–226.
32 M. Winter, J. O. Besenhard, M. E. Spahr and P. Novak, *Adv. Mater.*, 1998, **10**, 725–763.
33 M. Matsumoto, R. R. Dasari, W. Ji, C. H. Feriante, T. C. Parker, S. R. Marder and W. R. Dichtel, *J. Am. Chem. Soc.*, 2017, **139**, 4999–5002.
34 S. Ruidas, B. Mohanty, P. Bhanja, E. S. Erakulan, R. Thapa, P. Das, A. Chowdhury, S. K. Mandal, B. K. Jena and A. Bhaumik, *ChemSusChem*, 2021, **14**, 5057–5506.
35 S. Mondal, R. Singuru, S. C. Shit, T. Hayashi, S. Irle, Y. Hijikata, J. Mondal and A. Bhaumik, *ACS Sustainable Chem. Eng.*, 2018, **6**, 1610–1619.
36 A. El-Faham, S. M. Osman, H. A. Al-Lohedan and G. A. El-Mahdy, *Molecules*, 2016, **21**, 714.
37 Y.-H. Yao, J. Li, H. Zhang, H.-L. Tang, L. Fang, G.-D. Niu, X.-J. Sun and F.-M. Zhang, *J. Mater. Chem. A*, 2020, **8**, 8949–8956.
38 C. Li, J. Yang, P. Pachfule, S. Li, M.-Y. Ye, J. Schmidt and A. Thomas, *Nat. Commun.*, 2020, **11**, 4712.
39 C. R. Deblase, K. Hernández-Burgos, K. E. Silberstein, G. G. Rodríguez-Calero, R. P. Bisbey, H. D. Abruña and W. R. Dichtel, *ACS Nano*, 2015, **9**, 3178–3183.
40 C. R. DeBlase, K. E. Silberstein, T. T. Truong, H. D. Abruna and W. R. Dichtel, *J. Am. Chem. Soc.*, 2013, **135**, 16821–16824.
41 M. C. Daugherty, E. Vitaku, R. L. Li, A. M. Evans, A. D. Chavez and W. R. Dichtel, *Chem. Commun.*, 2019, **55**, 2680–2683.
42 A. Dutta, A. K. Patra, S. Dutta, B. Saha and A. Bhaumik, *J. Mater. Chem.*, 2012, **22**, 14094–14100.
43 S. K. Kundu and A. Bhaumik, *RSC Adv.*, 2015, **5**, 32730–32739.
44 K. K. Halankar, B. P. Mandal, M. K. Jangid, A. Mukhopadhyay, S. S. Meena, R. Acharya and A. K. Tyagi, *RSC Adv.*, 2018, **8**, 1140–1147.
45 K. K. Halankar, B. P. Mandal, M. Jangid, A. Mukhopadhyay, N. Abharana, C. Nayakd, K. Dasgupta and A. K. Tyagi, *J. Alloys Compd.*, 2020, **844**, 156076.
46 K. K. Halankar, B. P. Mandal, S. Nigam, C. Majumder, A. P. Srivastava, R. Agarwal and A. K. Tyagi, *Energy Fuels*, 2021, **35**, 12556–12568.